

Research Article

Recyclable Xanthan/TiO₂ Composite Cryogels towards the Photodegradation of Cr(VI) Ions and Methylene Blue Dye

Paulo V. O. Toledo , Leandro R. Marques , and Denise F. S. Petri 

Institute of Chemistry, University of São Paulo, Av. Prof. Lineu Prestes 748, 05508-000 São Paulo, Brazil

Correspondence should be addressed to Denise F. S. Petri; dfsp@iq.usp.br

Received 26 October 2018; Accepted 2 January 2019; Published 10 February 2019

Academic Editor: De-Yi Wang

Copyright © 2019 Paulo V. O. Toledo et al. This is an open access article distributed under the Creative Commons Attribution License, which permits unrestricted use, distribution, and reproduction in any medium, provided the original work is properly cited.

Composite cryogels were prepared from xanthan gum (XG) precursor gels at 20 g L⁻¹ containing TiO₂ load at 5, 10, and 20 wt% and citric acid, as crosslinker. The effect of the pH over precursor gel on the properties of the resulting cryogels was evaluated. The characterization of the XG/TiO₂ cryogels comprised compression tests, swelling degree (SD) determination, Fourier transform infrared vibrational spectroscopy in the attenuated total reflectance mode (FTIR-ATR), scanning electron microscopy (SEM), and X-ray microtomography (CT) analyses. The largest compressive modulus (E) was observed for XG/TiO₂ 10% cryogels prepared at pH 4.0, which amounted to 100 ± 7 kPa, whereas the E value determined for bare XG cryogels was 29 ± 3 kPa. XG/TiO₂ 10% cryogels presented larger pores and thicker walls than bare XG cryogels, as evidenced by SEM and CT analyses. FTIR-ATR spectra evidenced the ester bonds stemming from the esterification among carboxylic acid groups and/or XG hydroxyl groups. XG/TiO₂ 10% cryogels presented SD of (61 ± 2) $g_{\text{water}}/g_{\text{cryogel}}$, long-term stability in water, and outstanding photocatalytic properties in the presence of Cr(VI) ions and methylene blue (MB). The photocatalytic processes for the reduction of Cr(VI) to Cr(III) and for the photobleaching of MB fitted the first-order kinetic model, yielding rate constants of 0.019 varying min⁻¹ and 0.0096 min⁻¹, respectively. For both processes, the XG/TiO₂ 10% cryogels could be recycled five times without losing shape or efficiency.

1. Introduction

Porous 3D polymer structures have a high surface area and low density, making them applicable as filters, catalysts, and insulators. A reliable way to produce 3D polymer structures is removing the solvent of a precursor gel of interest causing minimal damage to the original structure. When the solvent is exchanged by supercritical CO₂ and then CO₂ is eliminated by pressure decrease, the resulting monoliths are classified as aerogels [1]. When the precursor gel is frozen and the solvent is removed by freeze-drying, the monoliths are classified as cryogels [2]. Aerogels and cryogels can be tailored by choosing the material and synthesis that best fit the desired application [3, 4].

Composite cryogels are prepared by combining polymer and reinforcing particles to improve the mechanical, thermal, electric, magnetic, and catalytic properties. For instance, poly(*N*-isopropylacrylamide) cryogels reinforced with silica

nanoparticles presented superior mechanical and thermal behavior in comparison to bare poly(*N*-isopropylacrylamide) cryogels [5]. Polysaccharide/clay aerogels and cryogel composites are interesting because they are biodegradable systems. Some examples of successful biopolymer/clay porous structures are cellulose/clay [6, 7], casein/clay [8], alginate/clay [9], and xanthan gum/agar/clay [10].

Xanthan gum (XG) is produced at large scale by *Xanthomonas campestris* during the fermentation of monosaccharides [11]. It is a polysaccharide composed by D-glucosyl, D-mannosyl, and D-glucuronyl acid residues in a 2:2:1 molar ratio and variable proportions of *O*-acetyl and pyruvyl residues. Side chains consist of a trisaccharide composed of mannose (β -1,4) glucuronic acid (β -1,2) mannose attached to alternate glucose residues in the backbone by α -1,3 linkages [12]. Above pH 4.5, the D-glucuronic acid and pyruvyl residues are deprotonated, and XG chains behave as polyanions. Under these conditions, XG chains can form physical

or chemical networks either by interacting with polyvalent cations [13, 14] or by crosslinking with polyfunctional molecules, respectively [12]. Citric acid is an efficient nontoxic crosslinker for polysaccharides; the esterification reaction among the carboxylic acid groups and polysaccharide hydroxyl groups takes place upon heating at 165°C for seven min [15–17]. XG is biodegradable and biocompatible; for this reason, it is widely used in food and drug formulation [12, 18] and as scaffold for tissue engineering [19–23].

The combination of XG with inorganic particles improves the bioaffinity of XG scaffold, physical and chemical properties towards bare XG. For instance, XG/hydroxyapatite nanocomposites presented improved mechanical behavior [24, 25] and served as scaffolds for the proliferation of osteoblasts [24]. XG/montmorillonite in combination with chitosan [26] or agar [10] formed foams with superior mechanical properties. XG/bioglass hybrid scaffolds reinforced with cellulose nanocrystals presented improved mechanical stability in dry and wet states and good compatibility with osteoblasts [27]. XG/SiO₂ composites presented excellent mechanical properties and high capacity for the adsorption of methylene blue (MB) and Bismarck brown dyes [28]. Favorable interaction among XG chains and TiO₂ particles led to improved rheological behavior and interior wall coatings [29].

In the present study, composite cryogels of XG were prepared with different contents of TiO₂ P25 nanoparticles. The characterization of composite cryogels comprised compression tests, swelling degree determination, Fourier transform infrared vibrational spectroscopy in the attenuated total reflectance mode (FTIR-ATR), scanning electron microscopy (SEM), and X-ray microtomography (CT) analyses. The catalytic properties of XG/TiO₂ composite cryogels were tested upon immersion in aqueous solutions containing methylene blue (MB) or Cr(VI) ions under exposition of UV radiation. The photoinduced reaction showed better correlation with first-order kinetics model. The possibility of composite cryogels recycling was also evaluated. MB molecules and Cr(VI) ions were chosen because they can be found as pollutants in natural waters.

2. Materials and Methods

2.1. Materials. Xanthan gum, XG (Kelzan®, CP Kelco, Brazil, $M_v \sim 1.2 \times 10^6 \text{ g mol}^{-1}$), commercial titanium dioxide particles TiO₂ P25 (AEROXIDE®, Evonik, Brazil), citric acid (Labsynth, Brazil, 192.13 g mol⁻¹), and sodium hypophosphite (Labsynth, Brazil, 87.98 g mol⁻¹) were used as received. The chemical structures of XG and citric acid are provided in Figures 1(a) and 1(b), respectively. Hydrochloric acid (Labsynth, Brazil, 1.17 g mL⁻¹, 37%, 36.46 g mol⁻¹) and sodium hydroxide (Labsynth, Brazil, 40.00 g mol⁻¹) were used to adjust solutions pH during synthesis and long-term stability tests. Solutions of potassium dichromate (Labsynth, Brazil, 294.18 g mol⁻¹) and methylene blue (M9140, Sigma-Aldrich, 319.85 g mol⁻¹) were used to test the catalysis effectiveness of hybrid cryogels under UVC light.

2.2. Synthesis of Composite Cryogels. Figure 1(c) shows schematically the preparation of composite cryogels. First, TiO₂

particles were dispersed in Milli-Q water at 1.0 g L⁻¹, 2.0 g L⁻¹, or 4 g L⁻¹ under magnetic stirring for 30 min. Then, XG, citric acid (crosslinker), and sodium hypophosphite (catalyst) were added to the TiO₂ dispersions, so that their final concentrations amounted to 20 g L⁻¹, 1.0 g L⁻¹, and 0.5 g L⁻¹, respectively. The contents of TiO₂ particles in relation to the XG mass amounted to 5%, 10%, or 20%. The pH was adjusted to 2, 4, or 7 by adding droplets of HCl 0.1 mol L⁻¹ or NaOH 0.1 mol L⁻¹. After 8 h under magnetic stirring, the precursor composite gels were kept in the refrigerator at 7°C overnight. As control, XG cryogels were prepared in the absence of TiO₂ particles.

The precursor gels were poured either into rectangular polypropylene molds (25 mm × 17 mm × 13 mm) for mechanical tests, cylindrical acrylic molds of 10 mm diameter and 6 mm high for morphological analyses, or polystyrene Petri dish 35 mm diameter and 2 mm high for the catalytic assays. The photographs of molds and resulting cryogels are presented as Supplementary Material SM1. The samples were frozen during 2 hours in a standard freezer at -25°C, followed by 24 h of freeze-drying. After that, the cryogels were withdrawn from the molds and heated for 7 min at 165°C to promote the esterification among citric acid and hydroxyl groups from XG chains [17]. The resulting cryogels were rinsed with Milli-Q water in order to remove unreacted molecules and freeze-dried again; they were coded as XG, XG/TiO₂ 5%, XG/TiO₂ 10%, and XG/TiO₂ 20%.

2.3. Characterization. The X-ray diffractograms (XRD) of TiO₂ particles were recorded with a Rigaku Miniflex diffractometer (Tokyo) operating at 30 kV, 15 mA, and $\lambda (\text{CuK}\alpha) = 0.154 \text{ nm}$, $0.5^\circ \text{ min}^{-1}$, sampling width of 0.010° , at room temperature in the 2θ range between 10° and 90° . Dynamic light scattering (DLS) measurements were performed in a Zetasizer Nano-ZS90 Malvern equipment with a He-Ne laser operating at 632.8 nm at $23 \pm 1^\circ \text{C}$ for dispersions of TiO₂ at 0.01 wt%, pH 7.0, pH 4.0, and pH 2.0 after five min equilibration. The average particle diameter (z -average, D_z) and polydispersity (PDI) of each sample were calculated using the cumulant method for the corresponding autocorrelation function. The D_z and PDI values represent the mean values for triplicates. Scanning electron microscopy (SEM) analyses were performed in a Jeol microscope FEG7401F equipped with a field-emission gun operating at voltage of 3 kV. Droplets of diluted dispersion of TiO₂ were deposited on clean Si wafers and allowed to dry at 40°C overnight.

The apparent density (ρ_{ap}) of composite cryogels was determined by weighing them in an analytical balance and measuring their dimensions with a pachometer over ten samples at $22 \pm 1^\circ \text{C}$ and relative humidity of $60 \pm 10\%$. The swelling degree (SD) was determined with a precision tensiometer Krüss K100 at $22 \pm 1^\circ \text{C}$ and relative humidity of $65 \pm 5\%$. The SD was calculated as the mass of sorbed water after 10 min divided by the mass of dried adsorbent, which was in average $12 \pm 1 \text{ mg}$. Fourier transform infrared vibrational spectroscopy in the attenuated total reflectance mode (FTIR-ATR) spectra were obtained with a PerkinElmer Frontier with Zn/Se crystal equipment with resolution of 4 cm^{-1} and in

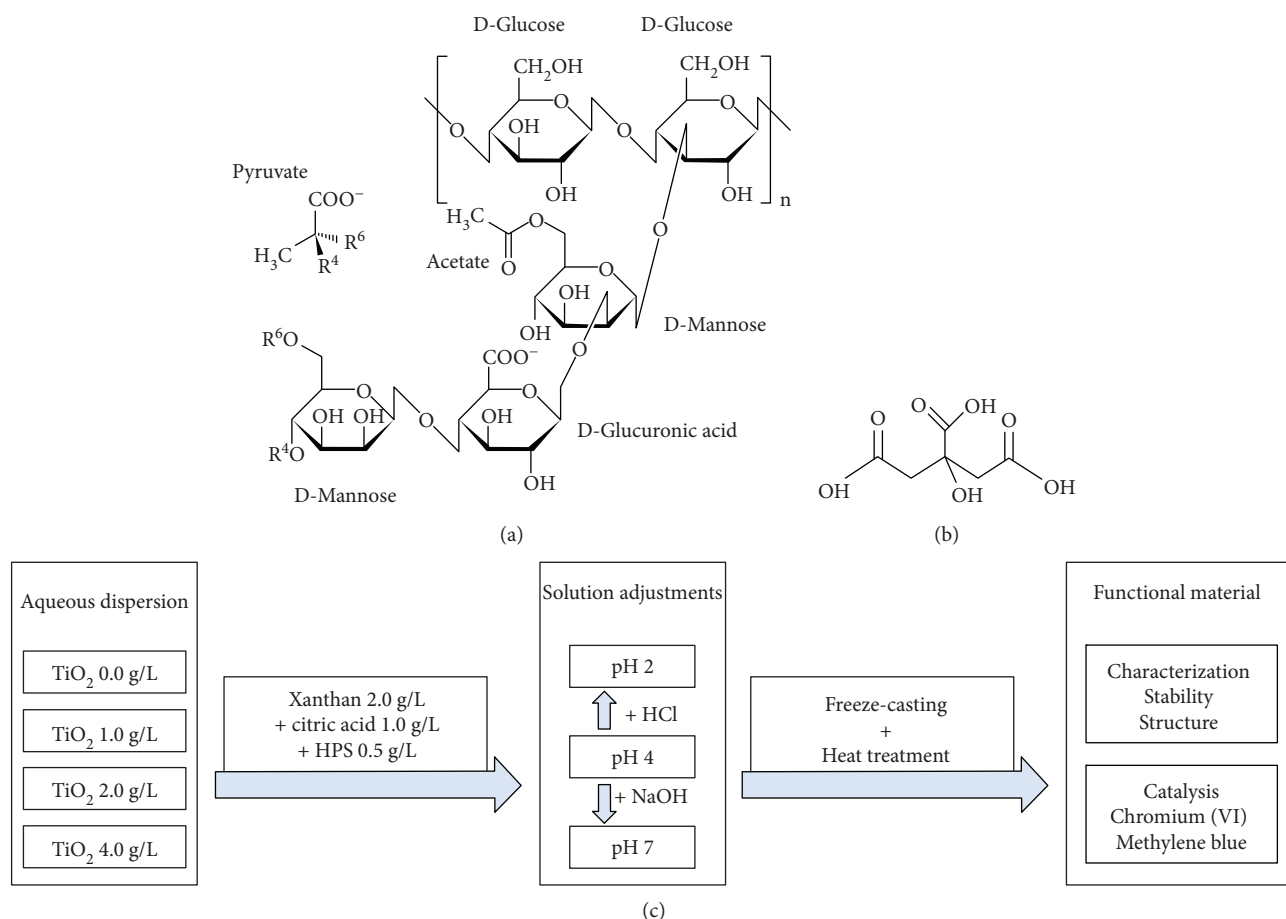


FIGURE 1: Schematic representation of (a) XG and (b) citric acid chemical structures and (c) hydrogels and cryogels preparation for further characterization and adsorption studies.

the range of 600 cm^{-1} to 4000 cm^{-1} . Compression tests were performed with a digital dynamometer IP 90DI-10 with a load cell of 10.0N, limit of applied force of 0.1 N, accuracy of 0.5% at $22 \pm 1^\circ\text{C}$, and relative humidity of $60 \pm 10\%$. SEM analyses were conducted with a JEOL Neoscope JCM 5000 equipment, operating at voltage of 10kV, on samples coated by sputtering with 5 nm of gold. X-ray microtomography (CT) analyses were performed with a Skyscan 1272 Bruker equipment, operating at 20kV and $175\ \mu\text{A}$. The sample was rotated stepwise (0.6° per step) through 360° , and images were recorded at each step with an exposure time of 5 s, yielding spatial resolution of $10\ \mu\text{m}$. In average, 600 X-ray images were taken in 60 min, scanning along the whole sample, yielding images with spatial resolution of $10\ \mu\text{m}$. The thresholding of the calculated gray scale images (from 13 to 255) and the transformation of the CT data into microstructural parameters were performed for all samples in the same way, using the CTAn Bruker software.

2.4. Photoreduction of Cr(VI) and Methylene Blue (MB). Discs of cryogels (2 mm high, 35 mm diameter, $\sim 0.050\text{ g}$) were inserted in Petri dishes (55 mm diameter) containing 5 mL of 120 mg L^{-1} ($4 \times 10^{-4}\text{ mol L}^{-1}$) $\text{K}_2\text{Cr}_2\text{O}_7$ solution at pH 1.0 or 2.0. As a control experiment, pieces of bare XG

cryogels were tested under the same conditions. The systems were arranged equidistant from an UVC lamp (Osram 36 W, 265 nm at 10 cm of the bulb), which was mounted in the center of a closed box (Supplementary Material SM2). The systems were irradiated during 15 min, then an aliquot of 1 mL was withdrawn for the quantification of Cr(VI) in the solution by means of spectrophotometry at 434 nm (Beckman-Coulter DU650 spectrophotometer), which is a wavelength for the maximal absorbance. After absorbance reading, which took less than one minute, the aliquot was returned to the Petri dish. The procedure was repeated 6 times, totalizing 90 minutes of irradiation. The reduction of Cr(VI) to Cr(III) was monitored using as reference the absorbance of the initial $4 \times 10^{-4}\text{ mol L}^{-1}$ $\text{K}_2\text{Cr}_2\text{O}_7$ solution, which was not irradiated and was kept in the absence of UV irradiation.

Discs of cryogels (2 mm high, 35 mm diameter, $\sim 0.050\text{ g}$) were inserted in Petri dishes (55 mm diameter) containing 5 mL of 5.0 mg L^{-1} ($15.6\ \mu\text{mol L}^{-1}$) MB solution prepared in 50 mM Tris-HCl, pH 7.0 [30]. At this, pH MB molecules are positively charged [31]. As a control experiment, pieces of bare XG cryogels were tested under the same conditions. The systems were irradiated during 15 min, and then an aliquot of 1 mL was withdrawn for the quantification of MB

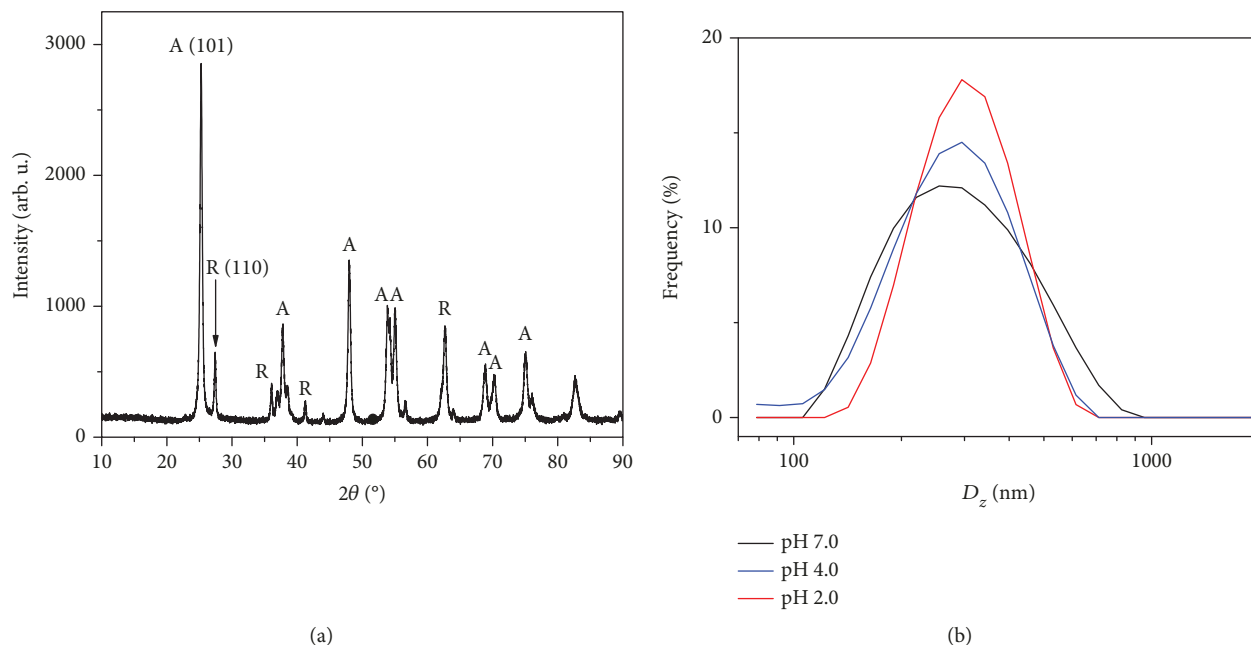


FIGURE 2: (a) X-ray diffractogram and (b) size distribution determined for TiO₂ P25 particles.

in the solution by means of spectrophotometry at 664 nm, which is a wavelength for the maximal absorbance. After absorbance reading, the aliquot was returned to the Petri dish. The procedure was repeated 8 times, totalizing 120 minutes of irradiation. The photobleaching of MB was monitored using the initial MB solution ($\sim 17 \mu\text{mol L}^{-1}$), which was not irradiated and was kept in the absence of UV irradiation.

3. Results and Discussion

3.1. Characterization of TiO₂ Particles. Figure 2(a) shows the X-ray diffractogram obtained for TiO₂ P25 particles. It presents typical diffraction peaks of anatase and rutile isomorphous forms. The weight percentages of anatase and rutile, X_A and X_R , respectively, were estimated using the Spurr-Myers equations [32].

$$\begin{aligned} X_A(\%) &= \frac{100}{(1 + 1.265(I_R/I_A))}, \\ X_R(\%) &= \frac{100}{(1 + 0.8(I_A/I_R))}, \end{aligned} \quad (1)$$

where I_A and I_R are the intensity of anatase peak at $2\theta = 25.25^\circ$ (101) and the intensity of rutile peak at $2\theta = 27.42^\circ$ (110). The contents of anatase and rutile amounted to 77% and 23%, respectively, which are in agreement with literature values [33].

Figure 2(b) shows the size distribution determined for TiO₂ P25 particles dispersed at pH 7.0, pH 4.0, and pH 2.0, the mean D_z values amounted to (344 ± 15) nm, (289 ± 8) nm, and (281 ± 4) nm, respectively, and the mean PDI values amounted to 0.45 ± 0.06 , 0.28 ± 0.03 , and

0.31 ± 0.04 , respectively. The average sizes of the anatase and rutile elementary particles are 85 nm and 25 nm, respectively [34]. Thus, the observed D_z values probably correspond to the aggregates of TiO₂ P25. Moreover, the experimental D_z data indicated that at pH 7.0, the particles tend to form larger aggregates because it is close to the isoelectric point (pI) of TiO₂ P25, which is reported as 6.2 [35], whereas at pH 4.0 or 2.0, they presented similar mean D_z values. SEM images obtained for TiO₂ P25 particles dispersed at pH 2.0 were provided as Supplementary Material SM3, they revealed the predominance of particles with mean size of (30 ± 5) nm and aggregates ranging from 100 nm to 500 nm in agreement with the D_z values.

3.2. Characterization of Composite Cryogels. In order to evaluate the effect of TiO₂ content in the cryogels on the compressive modulus, all cryogels were prepared at pH 4.0 because at this pH no tendency of particle aggregation was observed (Figure 2(b)). Typical compressive stress-strain curves determined for bare XG cryogels and XG/TiO₂ cryogels with 5%, 10%, and 20% TiO₂ prepared at pH 4.0 are presented in the Supplementary Material Figure SM4; the corresponding Young compressive modulus (E) values were determined from the slopes of linear regions. Figure 3 shows that the mean E values increased with the increase of TiO₂ content in the cryogels up to 10%, where the maximum E value achieved 100 ± 7 kPa. Similar behavior was observed for TiO₂ in epoxy composites [36] and cellulose nanocrystals in cellulose acetate butyrate composites [37]. A possible explanation for this effect is that for TiO₂ contents larger than 10%, the dispersion of the filler in the matrix is no longer effective, reducing the compressive strength.

In order to evaluate the effect of the precursor pH on the physicochemical properties of resulting cryogels, the

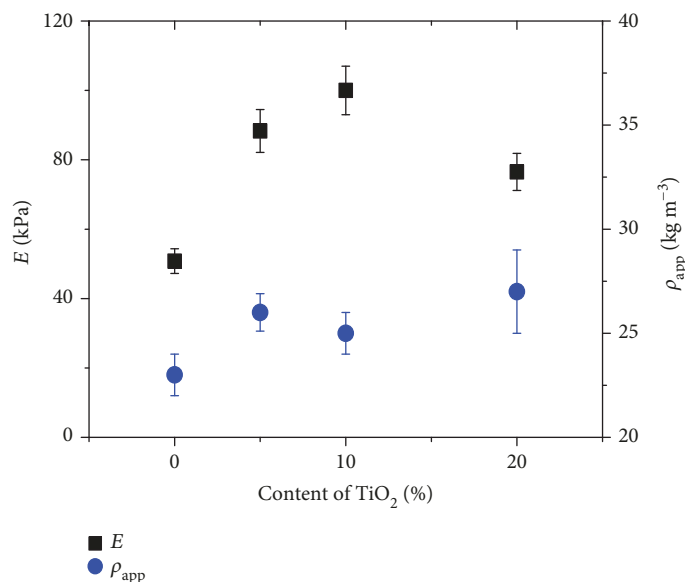


FIGURE 3: Dependence of compression modulus (E) and apparent density on the TiO_2 content in the composites from precursors prepared at pH 4.0. The data represent mean values and standard deviations of triplicate.

TABLE 1: Compression modulus (E) and density (ρ_{app}) values determined for bare XG and XG/ TiO_2 10% cryogels prepared at pH 2.0, 4.0, and 7.0. The data represent mean values and standard deviations of triplicate.

pH	E (kPa)		ρ_{app} (kg m^{-3})	
	XG	XG/ TiO_2 10%	XG	XG/ TiO_2 10%
2.0	30 ± 3	120 ± 8	24.0 ± 0.4	28 ± 1
4.0	29 ± 3	100 ± 7	23 ± 1	25 ± 1
7.0	29 ± 3	49 ± 3	23.8 ± 0.7	30 ± 1

composite cryogels were prepared with 10% TiO_2 at pH 2.0, 4.0, and 7.0. Table 1 shows the compression modulus (E) and apparent density (ρ_{app}) values determined for bare XG cryogels and XG/ TiO_2 10% prepared at pH 2.0, 4.0, and 7.0. The ρ_{app} values of bare XG or XG/ TiO_2 10% cryogels were not significantly affected by the precursor pH. However, the composite cryogels presented ρ_{app} values slightly higher than those determined for bare XG cryogels, due to the contribution of the dense TiO_2 particles.

The E values determined for the composite cryogels prepared at pH 2.0 or pH 4.0 were approximately fourfold and threefold that determined for bare XG cryogels, respectively. This interesting finding is in agreement with the observation that the addition of clay increased the ρ_{app} and E values of XG aerogel composites [10]. In general, for cellular materials, the E values are expected to increase if the ρ_{app} increase [38]. Thus, if the inorganic particles are well distributed in the polymeric matrix, increasing the composite density, the improvement of mechanical properties is expected [37].

The preparation of composite cryogels at pH 7.0 led to a drastic decrease of compressive modulus, indicating that at

pH 7.0 the interactions among TiO_2 particles and XG chains were weakened. At pH 7.0, the particles probably tend to aggregate due to the proximity to the pI of TiO_2 (6.2) [35], impairing the mechanical properties. The mean E value determined for XG/ TiO_2 10% composite cryogels prepared at pH 7 was almost twofold that obtained for bare XG cryogels. It was expected because the mean ρ_{app} value of composite cryogels was 1.3-fold larger than that of bare XG cryogels.

Figure 4 shows the SEM images obtained for bare XG and XG/ TiO_2 10% cryogels prepared at pH 2.0, 4.0, and 7.0. All cryogels presented isotropic open cells, regardless of the pH or composition. Bare XG hydrogels prepared from precursors containing acetic acid or hydrochloric acid presented similar morphological features [39]. The composite cryogels presented in average larger pores than the bare XG cryogels. In order to gain insight about the morphometric parameters, microtomography (CT) analyses were performed for XG and XG/ TiO_2 10% cryogels prepared at pH 4.0. Figure 5 and Table 2 show the typical reconstructed CT images and the corresponding morphometric parameters. Table 2 shows that the ρ_{app} values calculated from CT analyses were similar to those calculated by dividing the mass by the volume presented in Table 1. XG and XG/ TiO_2 10% cryogels presented similar ρ_{app} , surface area (S), and porosity (P) values. However, the values of mean pore size (d) calculated for XG/ TiO_2 10% cryogels were larger than that for XG cryogels, in agreement with the SEM images in Figure 4. In average, the walls of XG/ TiO_2 10% cryogels were thicker ($h = 61 \mu\text{m}$) than those of XG cryogels ($h = 47 \mu\text{m}$), evidencing the integration of TiO_2 particles to the cryogels walls.

One potential application for TiO_2 hybrid composites is the photocatalytic reduction of pollutants present in aqueous media [40]. For this reason, the long-term stability in water was also investigated. Figure 6 shows photographs taken for XG and XG/ TiO_2 10% cryogels prepared at pH 2.0, 4.0, and

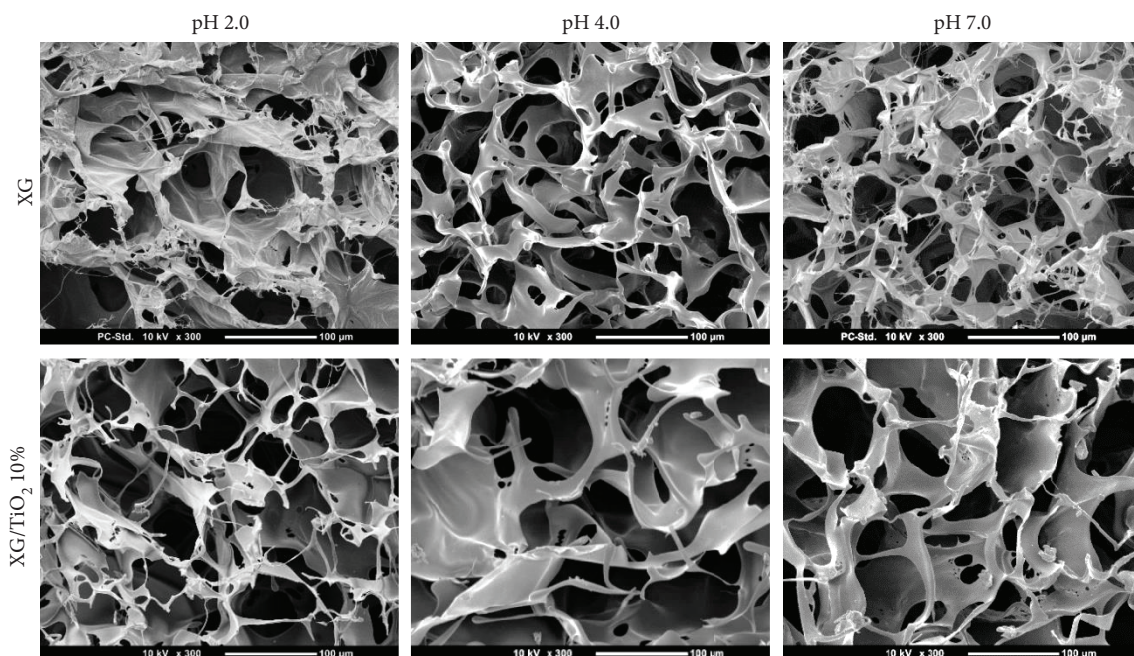


FIGURE 4: SEM images obtained for XG and XG/TiO₂ 10% cryogels prepared at pH 2.0, 4.0, and 7.0.

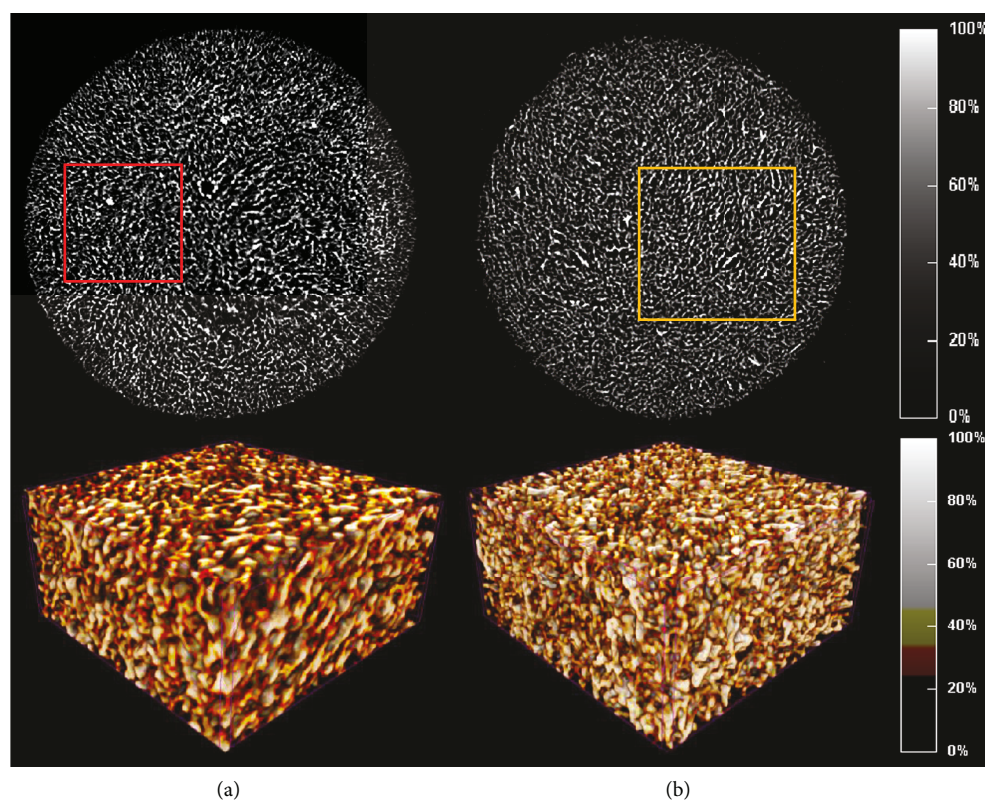


FIGURE 5: X-ray computer tomography images for (a) XG/TiO₂ 10% and (b) XG cryogels, which were prepared at pH 4.0 in molds of 7 mm and 5 mm diameter, respectively. Typical slices, from a total of 600 slices for each sample, are presented in the upper images. The reconstruction of 3D boxes (2 mm × 2 mm × 1 mm) was based on the slices and served for the morphometric analyses. The colors resulted from the transformation of the gray scale (red from 25% to 35% max attenuation, yellow from 35% to 45% attenuation, and white from 45% to 100%).

TABLE 2: Morphometric parameters from CT analyses: specific area (S), mean pore size (d), wall thickness (h), and integrated porosity (P) were determined for XG and XG/TiO₂ 10% cryogels.

Cryogel	Φ (mm)	ρ_{app} (kg m ⁻³)	S (m ² g ⁻¹)	d (μm)	h (μm)	P (%)
XG	5	24 ± 2	2.5 ± 0.1	39 ± 2	47 ± 1	93.2
XG/TiO ₂ 10%	7	26 ± 2	2.8 ± 0.4	45 ± 2	61 ± 1	93.8

7.0 just after immersion in Milli-Q water and after 7, 14, and 21 days in Milli-Q water. Just after immersion, only XG and XG/TiO₂ 10% cryogels prepared at pH 2.0 or pH 4.0 kept their original form; those prepared at pH 7.0 swollen and dissolved. This behavior corroborates with the low compressive strength observed for the XG/TiO₂ 10% cryogels prepared at pH 7.0 (Table 1), which was attributed to weak interaction among XG chains and TiO₂ particles. If the TiO₂ particles were intimately attached to the XG chains, the cryogels would have higher E value and better stability in water.

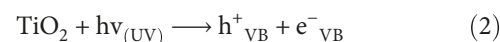
After seven days in contact with Milli-Q water, the cryogels prepared at pH 2.0 or 4.0 swollen but did not dissolve, whereas those synthesized at pH 7.0 dissolved completely. After 14 or 21 days in contact with water, the XG cryogels prepared at pH 2.0 or 4.0 remained the same. On the other hand, after 14 or 21 days, the XG/TiO₂ 10% cryogels prepared at pH 2.0 presented fungi on the surface, whereas those prepared at pH 4.0 were completely free of fungi and the supernatant turned turbid, indicating that TiO₂ particles were partially released to the medium, avoiding fungi proliferation. The antimicrobial properties of TiO₂ particles are well described in the literature [41]; one possible mechanism is the peroxidation and decomposition of fatty acids present in the bacteria membrane cell by the photoactivity of TiO₂ particles [42].

The esterification among citric acid molecules and XG chains were favored at pH 2.0 or 4.0 because the carboxylic acid groups are protonated [16, 17]. At pH 7.0, the esterification was not possible due to the deprotonation of XG and citric acid groups. Considering the pI of TiO₂ P25 at pH 6.2 [35], at pH 2.0 or 4.0 the particles surface is enriched by the Ti-O-H groups, which can undergo esterification with the carboxylic acid groups from citric acid and XG chains. The photographs showed that composite cryogels prepared at pH 4.0 remained stable in water for a long time, but the supernatant became slightly turbid, indicating that some TiO₂ particles were not efficiently bound to the matrix. At pH 7.0, the esterification among XG and citric acid or TiO₂ particles was not favored due to deprotonation; consequently, the cryogels presented low compressive strength and no stability in water.

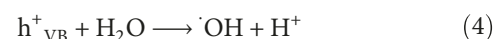
Typical water sorption curves recorded during 10 min for the determination of swelling degree (SD) of XG and XG/TiO₂ 10% cryogels prepared at pH 4.0 are presented as Supplementary Material SM5. The SD values of XG and XG/TiO₂ 10% cryogels amounted to $(57 \pm 2) g_{\text{water}}/g_{\text{cryogel}}$ and $(61 \pm 2) g_{\text{water}}/g_{\text{cryogel}}$, respectively, evidencing similar affinity for water.

Figure 7(a) shows the FTIR-ATR spectra obtained for TiO₂ P25 (powder), XG (powder), and XG and XG/TiO₂ 10% cryogels prepared at pH 4.0. The complete band assignment is presented as Supplementary Material Table SM1. Briefly, a broad band from 3500 to 3000 cm⁻¹ appeared in all spectra, it was attributed to O-H stretching. Except for the TiO₂ P25 (powder) spectrum, the C-H stretching band at 2910 cm⁻¹ was present in all spectra. The spectral region from 1100 to 1800 cm⁻¹ was shown in Figure 7(b). The most important feature is that the ester bonds resulting from the esterification among citric acid carboxylic acid groups and/or XG hydroxyl groups were evidenced by the appearance of the band at 1725 cm⁻¹ in the FTIR-ATR spectra determined for XG and XG/TiO₂ 10% cryogels which was attributed to C=O axial deformation; noteworthy, this band was absent in the XG (powder) [16].

3.3. Photocatalytic Properties of Cryogels. The photocatalytic properties of XG and XG/TiO₂ 10% cryogels prepared at pH 4.0 were evaluated in the reduction of Cr(VI) to Cr(III) ions and in the photobleaching of methylene blue (MB), under exposition of UV radiation. Control experiments were conducted in the dark. The irradiation of TiO₂ with UV light results in photon absorption and excitation of an electron (e^-_{VB}) from valence band (VB) to the conduction band (CB), thereby generating a positive electron hole in the valence band (h^+_{VB}) [43]:



The e^-_{VB} and h^+_{VB} species are present on the TiO₂ particles surface. The e^-_{VB} can react with O₂ to form superoxide radicals or hydroperoxide radicals, and the h^+_{VB} can react with water, generating hydroxyl radicals:



Under acid conditions, the reduction of Cr(VI) to Cr(III) follows:

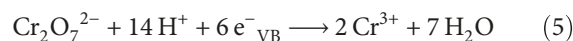


Figure 8 shows the decrease of Cr(VI) concentration as a function of time at pH 1.0 and 2.0. In order to increase the contact area of the cryogels with the Cr(VI) ions in solution, the cryogels were prepared as discs (about 2 mm thick, 35 mm diameter) and immersed in the solution. The reduction of Cr(VI) to Cr(III) was observed in solutions, which were in contact with XG and XG/TiO₂ 10% cryogels. In both situations, the experimental data were better fitted with the first-order (Figures 8(b) and 8(d)) model than with the second-order (Supplementary Material SM6) model, in agreement with the photoreduction of Cr(VI) by pure TiO₂ particles [44]. Table 3 presents the fitting parameters. At pH 2.0, the rate constants were similar in both cases, whereas at pH 1.0 the reduction rate was slightly larger for XG/TiO₂

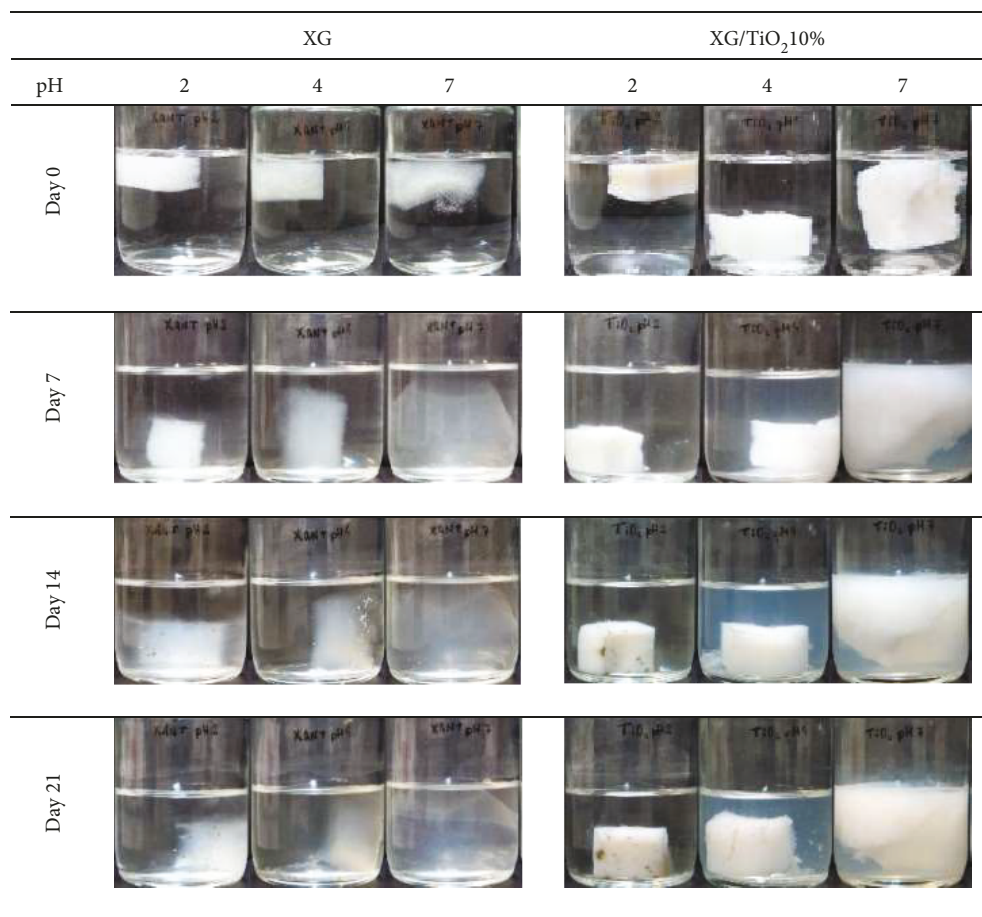


FIGURE 6: Photographs of XG and XG/TiO₂ 10% cryogels prepared at pH 2.0, 4.0, and 7.0 just after immersion (day 0) in Milli-Q water and after 7, 14, and 21 days immersed in Milli-Q water.

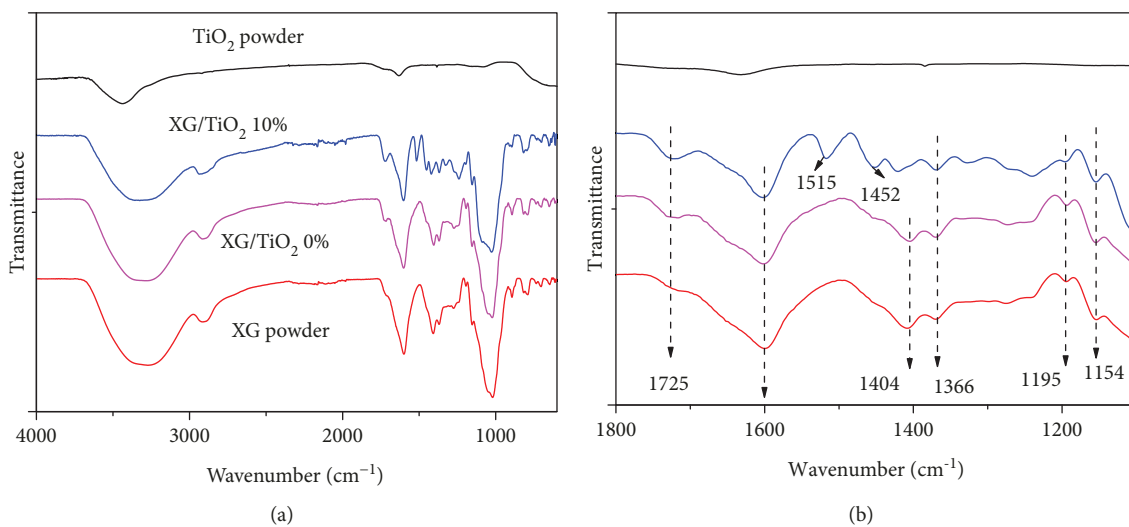


FIGURE 7: FTIR-ATR spectra obtained for TiO₂ P25 (powder), XG (powder), and XG and XG/TiO₂ 10% cryogels prepared at pH 4.0.

10% than for XG cryogels. The rate constants in Table 3 are large in comparison to those reported for pure TiO₂, for instance, at pH 2 the k value is reported as 0.00373 min^{-1}

[44], five times smaller than those determined for XG/TiO₂ 10% cryogels. The efficiency of bare XG cryogels is due the reducing ends of XG chains. Efficient reduction of Cr(VI)

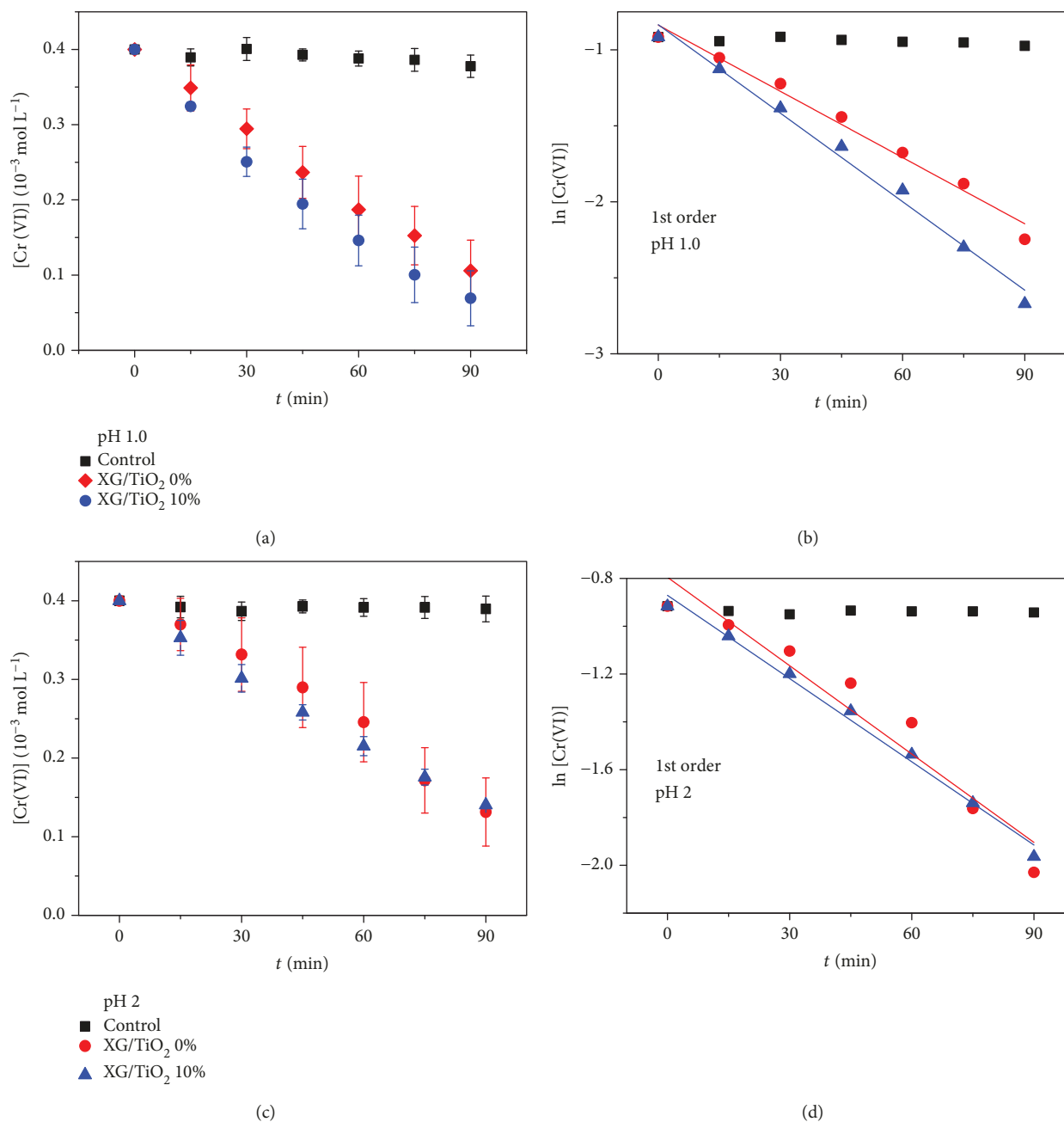


FIGURE 8: Decrease of initial concentration of Cr(VI) ions ($4 \times 10^{-4} \text{ mol L}^{-1}$) as a function of time upon contact with XG (red symbol) or XG/TiO₂ 10% (blue symbol) cryogels at $25 \pm 1^\circ\text{C}$ and (a) pH 1.0 and (c) pH 2.0. Fittings to first-order kinetic model for the experimental data at (b) pH 1.0 and (d) pH 2.0. The control experiment was done in the absence of cryogels.

ions to Cr(III) ions was also observed for alginate [45] and chitosan [46] matrices.

The mechanism for the photodegradation of methylene blue (MB) molecules mediated by TiO₂ under UV radiation is well reported in the literature [47]. The MB molecules react with the reactive oxygen species (ROS) in equations (3) and (4), resulting in CO₂, H₂SO₄, and HNO₃ and as final products [47]. Figure 9(a) shows the decrease of MB concentration as a function of time at pH 7.0 (Tris-HCl buffer), the crygel discs were immersed in the MB solutions while the systems were irradiated. The experimental data fitted better

the first-order model (Figure 9(b)) than the second-order model (Supplementary Material SM7), as evidenced by the R^2 values in Table 3. The k^1 value determined for the photodegradation of MB with XG/TiO₂ 10% cryogels was twice the k^1 value determined for bare XG cryogels and 10 times k^1 value determined for the control, evidencing the catalytic efficiency of the composite cryogels. The k^1 values determined for the photobleaching of MB in contact with TiO₂ P25 and under laser pulse with 50, 100, 150, and 200 mJ energy amounted to 0.00433, 0.00519, 0.00741, and 0.00577 min^{-1} , respectively [48]; the k^1 values were similar to that

TABLE 3: Fitting parameters to first-order and second-order kinetic models corresponding to the reduction of Cr(VI) to Cr(III) at pH 1.0 and pH 2.0 and to the photodegradation of MB at pH 7.0 (Tris-HCl buffer) in the presence of XG or XG/TiO₂ 10% cryogels. The control experiment was done in the absence of cryogels.

Medium pH	Cryogel	1st order		2nd order	
		k^1 (min ⁻¹)	R^2	k^2 (L mol ⁻¹ min ⁻¹)	R^2
Cr(VI) reduction					
1.0	XG	0.015	0.9780	72	0.8766
	XG/TiO ₂ 10%	0.019	0.9867	125	0.8615
2.0	XG	0.012	0.9229	54	0.8267
	XG/TiO ₂ 10%	0.012	0.9898	50	0.9318
MB photodegradation					
7.0	XG	0.0046	0.9552	704	0.8924
	XG/TiO ₂ 10%	0.0096	0.9971	2304	0.9752
	Control	0.0009	0.8651	93	0.8828

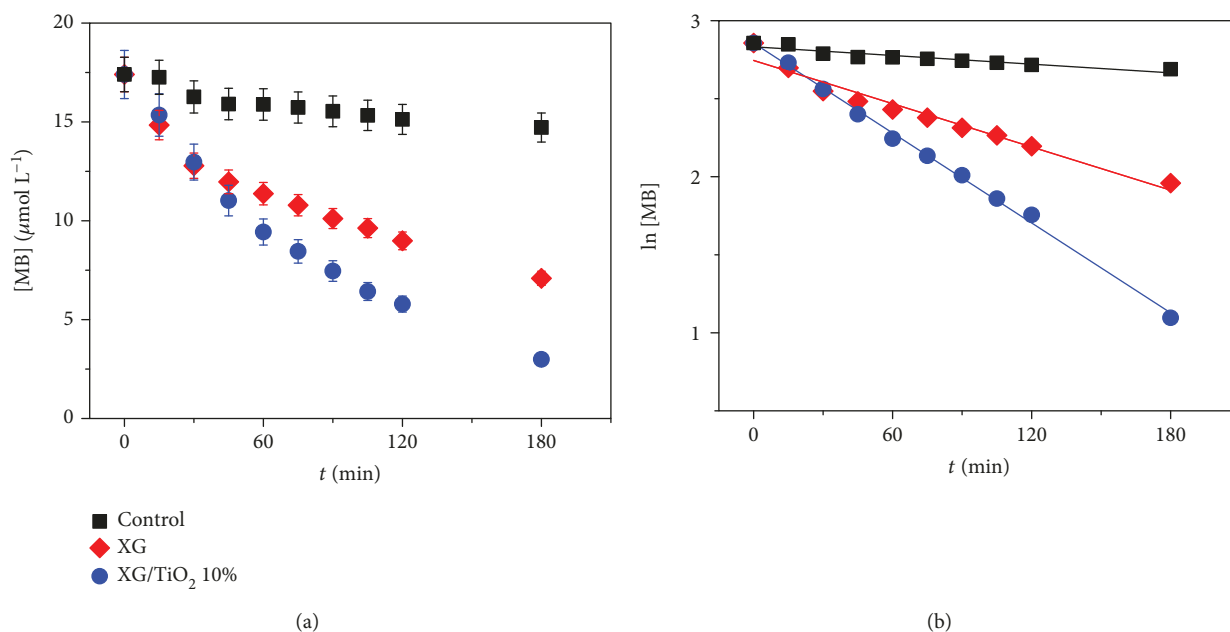


FIGURE 9: (a) Decrease of initial concentration of MB ($17.5 \mu\text{mol L}^{-1}$) as a function of time upon contact with XG (red symbol) or XG/TiO₂ 10% (blue symbol) cryogels at $25 \pm 1^\circ\text{C}$. (b) Fittings to first-order kinetic model. The control experiment was done in the absence of cryogels.

determined for bare XG cryogels. The control experiment was done in the absence of cryogels.

The initial concentration of MB was reduced by 46% and 95% upon contact with XG/TiO₂ 10% cryogels under UV radiation after 60 min and 5.2 h, respectively. For comparison, under optimum conditions, hydrogels of poly(acrylic acid) crosslinked with N,N-methylene bis-acrylamide (MBA), and TiO₂ reduced 95% of the initial MB concentration after 5 h under sunlight radiation [49]. In order to illustrate the photocatalytic effect of TiO₂ in the composites cryogels, 1 mL of MB solution at $7.8 \cdot 10^{-4} \text{mol L}^{-1}$ was added to bare XG and XG/TiO₂ 10% cryogels, irradiated by UV for 2 h. Figure 10 shows the photographs of XG and XG/TiO₂ 10% before the addition of MB solution, just after the addition of MB solution, after 1 h and 2 h of UV radiation; the

photographs clearly showed the catalytic effect of TiO₂ on the photodegradation of MB.

The possibility of recycling the XG/TiO₂ 10% cryogels was evaluated. After the photoreduction of Cr(VI) or photodegradation of MB, they were rinsed with the corresponding solvents (HCl or Tris-HCl buffer) and reused without losing the original shape or efficiency for five times.

4. Conclusions

The results presented in this study evidenced that the TiO₂ P25 particles enhanced the mechanical and catalytic properties of XG cryogels. The pH of the precursor gel played a crucial role on the chemical stability and mechanical properties of composite cryogels. Close to the pI of TiO₂ particles

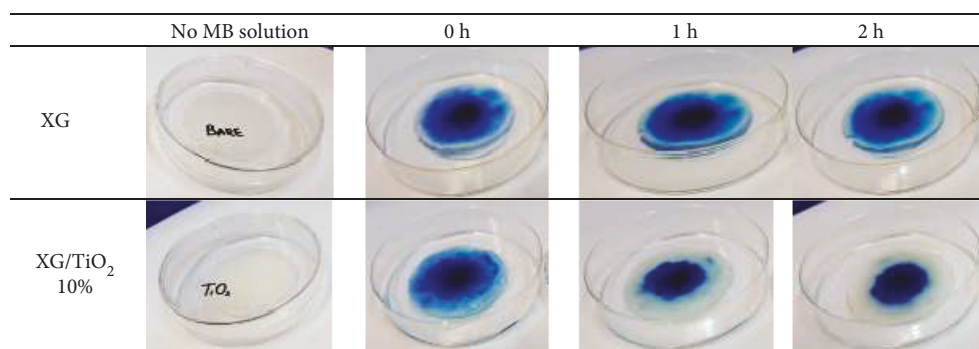


FIGURE 10: Photographs of XG and XG/TiO₂ 10% cryogels before the addition of MB solution, just after the addition of MB solution (0 h), after 1 h and 2 h of UV radiation.

(pH 7), the interactions among XG chains and particles were not favored, yielding weak cryogels. On the other hand, the precursor preparation at pH 2 or pH 4 favored the interactions among XG hydroxyl and carboxylic acid groups and TiO₂ particles by H bonding. The outstanding mechanical properties and stability in water enabled the application of XG/TiO₂ 10% as adsorbents for pollutants present in aqueous media. Their efficiency in the reduction of Cr(VI) to Cr(III) ions and in the degradation of MB, upon UV radiation, could be attested in repeated cycles, without losing the original shape. Thus, the XG/TiO₂ 10% cryogels displayed mechanical and catalytic properties, which evidenced their potential as environmentally friendly adsorbents.

Data Availability

The data used to support the findings of this study are included within the supplementary information file.

Conflicts of Interest

The authors declare that there is no conflict of interest regarding the publication of this paper.

Acknowledgments

We acknowledge Talita de Francesco Calheiros for the assistance with the DLS measurements. This work was supported by Conselho Nacional de Desenvolvimento Científico e Tecnológico (CNPq Grants 306848/2017 and 421014/2018-0). We also thank LNNano-CNPEM (Project Micro CT-22728, Campinas, Brazil) for the microtomography measurements. This study was financed in part by the Coordenação de Aperfeiçoamento de Pessoal de Nível Superior, Brazil (CAPES) - Finance Code 001.

Supplementary Materials

Figure S1: photographs of molds used and the resulting cryogels. Figure S2: experimental setup for the photocatalytic experiments. Figure S3: typical SEM images of TiO₂ P25 particles. The particles were not coated with gold prior to the analyses because they are semiconductor. The mean size of TiO₂ particles amounted to (30 ± 5) nm, as an average

of 15 measurements (red lines). The aggregates ranged from 100 nm to 500 nm, in agreement with the D_z values. Figure S4: typical compressive stress- (σ -) strain curves determined for bare XG cryogels (0%) and XG/TiO₂ cryogels with 5%, 10%, and 20% TiO₂ prepared at pH 4. Figure S5: typical Milli-Q water sorption curves determined for XG and XG/TiO₂ 10% cryogels prepared at pH 4. Figure S6: fittings to second-order kinetic model for the experimental data of reduction of Cr(VI) at (a) pH 1.0 and (b) pH 2.0 (see Figure 8). Figure S7: fittings to second-order kinetic model for the experimental data of degradation of MB at pH 7.0 (see Figure 9). Table S1: bands assignment regarding the FTIR spectra obtained for XG and TiO₂ powder and XG and XG/TiO₂ 10% cryogels. (*Supplementary Materials*)

References

- [1] I. Smirnova and P. Gurov, "Aerogels in chemical engineering: strategies toward tailor-made aerogels," *Annual Review of Chemical and Biomolecular Engineering*, vol. 8, no. 1, pp. 307–334, 2017.
- [2] N. Buchtova and T. Budtova, "Cellulose aero-, cryo- and xerogels: towards understanding of morphology control," *Cellulose*, vol. 23, no. 4, pp. 2585–2595, 2016.
- [3] S. Jiang, S. Agarwal, and A. Greiner, "Low-density open cellular sponges as functional materials," *Angewandte Chemie International Edition*, vol. 56, no. 49, pp. 15520–15538, 2017.
- [4] L. Y. Long, Y. X. Weng, and Y. Z. Wang, "Cellulose aerogels: synthesis, applications and prospects," *Polymers*, vol. 10, no. 6, p. 623, 2018.
- [5] O. Dogru, S. Abdurrahmanoglu, and N. Kayaman-Apohan, "Preparation and characterization of modified nanosilica/PNI-PAm hybrid cryogels," *Polymer Bulletin*, vol. 72, no. 5, pp. 993–1005, 2015.
- [6] A. Liu, L. Medina, and L. A. Berglund, "High-strength nanocomposite aerogels of ternary composition: poly(vinyl alcohol), clay, and cellulose nanofibrils," *ACS Applied Materials & Interfaces*, vol. 9, no. 7, pp. 6453–6461, 2017.
- [7] M. D. Gawryla, O. van den Berg, C. Weder, and D. A. Schiraldi, "Clay aerogel/cellulose whisker nanocomposites: a nanoscale wattle and daub," *Journal of Materials Chemistry*, vol. 19, no. 15, pp. 2118–2124, 2009.
- [8] T. Pojanavaraphan, R. Magaraphan, B. S. Chiou, and D. A. Schiraldi, "Development of biodegradable foamlike materials

- based on casein and sodium montmorillonite clay," *Biomacromolecules*, vol. 11, no. 10, pp. 2640–2646, 2010.
- [9] H. B. Chen, Y. Z. Wang, M. Sánchez-Soto, and D. A. Schiraldi, "Low flammability, foam-like materials based on ammonium alginate and sodium montmorillonite clay," *Polymer*, vol. 53, no. 25, pp. 5825–5831, 2012.
- [10] L. Wang, D. A. Schiraldi, and M. Sánchez-Soto, "Foamlike xanthan gum/clay aerogel composites and tailoring properties by blending with agar," *Industrial and Engineering Chemistry Research*, vol. 53, no. 18, pp. 7680–7687, 2014.
- [11] F. Garcia-Ochoa, V. E. Santos, J. A. Casas, and E. Gomez, "Xanthan gum: production, recovery, and properties," *Biotechnology Advances*, vol. 18, no. 7, pp. 549–579, 2000.
- [12] D. F. S. Petri, "Xanthan gum: a versatile biopolymer for biomedical and technological applications," *Journal of Applied Polymer Science*, vol. 132, no. 23, 2015.
- [13] A. F. Dario, L. M. A. Hortencio, M. R. Sierakowski, J. C. Queiroz Neto, and D. F. S. Petri, "The effect of calcium salts on the viscosity and adsorption behavior of xanthan," *Carbohydrate Polymers*, vol. 84, no. 1, pp. 669–676, 2011.
- [14] Z. H. Mohammed, A. Haque, R. K. Richardson, and E. R. Morris, "Promotion and inhibition of xanthan 'weak-gel' rheology by calcium ions," *Carbohydrate Polymers*, vol. 70, no. 1, pp. 38–45, 2007.
- [15] N. Reddy and Q. Yang, "Citric acid cross-linking of starch films," *Food Chemistry*, vol. 118, no. 3, pp. 702–711, 2010.
- [16] V. B. Bueno, R. Bentini, L. H. Catalani, and D. F. S. Petri, "Synthesis and swelling behavior of xanthan-based hydrogels," *Carbohydrate Polymers*, vol. 92, no. 2, pp. 1091–1099, 2013.
- [17] V. B. Bueno and D. F. S. Petri, "Xanthan hydrogel films: molecular conformation, charge density and protein carriers," *Carbohydrate Polymers*, vol. 101, pp. 897–904, 2014.
- [18] P. V. Bueno, K. C. P. Hilamatu, A. M. Carmona-Ribeiro, and D. F. S. Petri, "Magnetically triggered release of amoxicillin from xanthan/Fe₃O₄/albumin patches," *International Journal of Biological Macromolecules*, vol. 115, pp. 792–800, 2018.
- [19] A. Kumar, K. M. Rao, and S. S. Han, "Application of xanthan gum as polysaccharide in tissue engineering: a review," *Carbohydrate Polymers*, vol. 180, pp. 128–144, 2018.
- [20] V. B. Bueno, A. M. Silva, L. R. S. Barbosa et al., "Hybrid composites of xanthan and magnetic nanoparticles for cellular uptake," *Chemical Communications*, vol. 49, no. 85, pp. 9911–9913, 2013.
- [21] V. B. Bueno, S. H. Takahashi, L. H. Catalani, S. I. C. de Torresi, and D. F. S. Petri, "Biocompatible xanthan/polypyrrole scaffolds for tissue engineering," *Materials Science and Engineering: C*, vol. 52, pp. 121–128, 2015.
- [22] T. Glaser, V. B. Bueno, D. R. Cornejo, D. F. S. Petri, and H. Ulrich, "Neuronal adhesion, proliferation and differentiation of embryonic stem cells on hybrid scaffolds made of xanthan and magnetite nanoparticles," *Biomedical Materials*, vol. 10, no. 4, article 045002, 2015.
- [23] S. Kondaveeti, A. T. S. Semeano, D. R. Cornejo, H. Ulrich, and D. F. S. Petri, "Magnetic hydrogels for levodopa release and cell stimulation triggered by external magnetic field," *Colloids and Surfaces B: Biointerfaces*, vol. 167, pp. 415–424, 2018.
- [24] H. Izawa, S. Nishino, H. Maeda et al., "Mineralization of hydroxyapatite upon a unique xanthan gum hydrogel by an alternate soaking process," *Carbohydrate Polymers*, vol. 102, pp. 846–851, 2014.
- [25] V. B. Bueno, R. Bentini, L. H. Catalani, L. R. Barbosa, and D. F. S. Petri, "Synthesis and characterization of xanthan–hydroxyapatite nanocomposites for cellular uptake," *Materials Science and Engineering: C*, vol. 37, pp. 195–203, 2014.
- [26] H. Liu, K. Nakagawa, D. Chaudhary, Y. Asakuma, and M. O. Tadé, "Freeze-dried macroporous foam prepared from chitosan/xanthan gum/montmorillonite nanocomposites," *Chemical Engineering Research and Design*, vol. 89, no. 11, pp. 2356–2364, 2011.
- [27] A. Kumar, K. M. Rao, S. E. Kwon, Y. N. Lee, and S. S. Han, "Xanthan gum/bioactive silica glass hybrid scaffolds reinforced with cellulose nanocrystals: morphological, mechanical and in vitro cytocompatibility study," *Materials Letters*, vol. 193, pp. 274–278, 2017.
- [28] S. Thakur, S. Pandey, and O. A. Arotiba, "Sol-gel derived xanthan gum/silica nanocomposite a highly efficient cationic dyes adsorbent in aqueous system," *International Journal of Biological Macromolecules*, vol. 103, pp. 596–604, 2017.
- [29] H. Zhang, F. Tian, S. Chen, Q. Guo, F. Liu, and D. Sun, "Preparation of anatase nano-TiO₂/xanthan gum composite (NTX) and rheological study of the interior wall coatings using NTX as additive," *Pigment & Resin Technology*, vol. 40, no. 4, pp. 254–259, 2011.
- [30] B. F. Martins, P. V. O. Toledo, and D. F. S. Petri, "Hydroxypropyl methylcellulose based aerogels: synthesis, characterization and application as adsorbents for wastewater pollutants," *Carbohydrate Polymers*, vol. 155, pp. 173–181, 2017.
- [31] J. P. Tardivo, A. Del Giglio, C. C. Oliveira et al., "Methylene blue in photodynamic therapy: from basic mechanisms to clinical applications," *Photodiagnosis and Photodynamic Therapy*, vol. 2, no. 3, pp. 175–191, 2005.
- [32] R. A. Spurr and H. Myers, "Quantitative analysis of anatase-rutile mixtures with an X-ray diffractometer," *Analytical Chemistry*, vol. 29, no. 5, pp. 760–762, 1957.
- [33] L. White, Y. Koo, Y. Yun, and J. Sankar, "TiO₂ deposition on AZ31 magnesium alloy using plasma electrolytic oxidation," *Journal of Nanomaterials*, vol. 2013, Article ID 319437, 8 pages, 2013.
- [34] T. Ohno, K. Sarukawa, K. Tokieda, and M. Matsumur, "Morphology of a TiO₂ photocatalyst (Degussa, P-25) consisting of anatase and rutile crystalline phases," *Journal of Catalysis*, vol. 203, no. 1, pp. 82–86, 2001.
- [35] K. Suttiponparnit, J. Jiang, M. Sahu, S. Suvachittanon, T. Charinpanitkul, and P. Biswas, "Role of surface area, primary particle size, and crystal phase on titanium dioxide nanoparticle dispersion properties," *Nanoscale Research Letters*, vol. 6, no. 1, p. 27, 2010.
- [36] I. Ozsoy, A. Demirkol, A. Mimaroglu, H. Unal, and Z. Demir, "The influence of micro- and nano-filler content on the mechanical properties of epoxy composites," *Journal of Mechanical Engineering*, vol. 61, no. 11, pp. 601–609, 2015.
- [37] L. S. Blachechen, J. P. de Mesquita, E. L. de Paula, F. V. Pereira, and D. F. S. Petri, "Interplay of colloidal stability of cellulose nanocrystals and their dispersibility in cellulose acetate butyrate matrix," *Cellulose*, vol. 20, no. 3, pp. 1329–1342, 2013.
- [38] L. J. Gibson and M. F. Ashby, "Cellular solids: structure and properties," Cambridge University Press, 2nd edition, 1997.
- [39] P. V. O. Toledo and D. F. S. Petri, "Hydrophilic, hydrophobic, Janus and multilayer xanthan based cryogels," *International Journal of Biological Macromolecules*, vol. 123, pp. 1180–1188, 2019.

- [40] F. Ali, S. B. Khan, T. Kamal, K. A. Alamry, and A. M. Asiri, "Chitosan-titanium oxide fibers supported zero-valent nanoparticles: highly efficient and easily retrievable catalyst for the removal of organic pollutants," *Scientific Reports*, vol. 8, no. 1, p. 6260, 2018.
- [41] W. A. Daoud, J. H. Xin, and Y.-H. Zhang, "Surface functionalization of cellulose fibers with titanium dioxide nanoparticles and their combined bactericidal activities," *Surface Science*, vol. 599, no. 1-3, pp. 69-75, 2005.
- [42] U. Joost, K. Juganson, M. Visnapuu et al., "Photocatalytic antibacterial activity of nano-TiO₂ (anatase)-based thin films: effects on *Escherichia coli* cells and fatty acids," *Journal of Photochemistry and Photobiology B: Biology*, vol. 142, pp. 178-185, 2015.
- [43] S. Banerjee, S. C. Pillai, P. Falaras, K. E. O'Shea, J. A. Byrne, and D. D. Dionysiou, "New insights into the mechanism of visible light photocatalysis," *Journal of Physical Chemistry Letters*, vol. 5, no. 15, pp. 2543-2554, 2014.
- [44] Y. Ku and I.-L. Jung, "Photocatalytic reduction of Cr(VI) in aqueous solutions by UV irradiation with the presence of titanium dioxide," *Water Research*, vol. 35, no. 1, pp. 135-142, 2001.
- [45] G. G. A. de Carvalho, G. A. R. Kelmer, P. Fardim, P. V. Oliveira, and D. F. S. Petri, "Hybrid polysaccharide beads for enhancing adsorption of Cr(VI) ions," *Colloids and Surfaces A: Physicochemical and Engineering Aspects*, vol. 558, pp. 144-153, 2018.
- [46] Y. Zhang, S. Lin, J. Qiao et al., "Malic acid-enhanced chitosan hydrogel beads (mCHBs) for the removal of Cr(VI) and Cu(II) from aqueous solution," *Chemical Engineering Journal*, vol. 353, pp. 225-236, 2018.
- [47] R. Zuo, G. Du, W. Zhang et al., "Photocatalytic degradation of methylene blue using TiO₂ impregnated diatomite," *Advances in Materials Science and Engineering*, vol. 2014, Article ID 170148, 7 pages, 2014.
- [48] Z. H. Yamani, "Comparative study on photocatalytic degradation of methylene blue by Degussa P25 titania: pulsed laser light versus continuous broad spectrum lamp irradiation," *Arabian Journal for Science and Engineering*, vol. 43, no. 1, pp. 423-432, 2017.
- [49] F. Kazemi, Z. Mohamadnia, B. Kaboudin, and Z. Karimi, "Photodegradation of methylene blue with a titanium dioxide/polyacrylamide photocatalyst under sunlight," *Journal of Applied Polymer Science*, vol. 133, no. 19, 2016.

